

Mapping the conformational energy landscape of Abl kinase using ClyA nanopore tweezers

Fanjun Li

University of Massachusetts Amherst

Monifa Fahie

University of Massachusetts Amherst

Kaitlyn Gilliam

University of Massachusetts Amherst

Ryan Pham

University of Massachusetts Amherst

Min Chen (✉ mchen1@chem.umass.edu)

University of Massachusetts Amherst <https://orcid.org/0000-0002-7572-0761>

Article

Keywords:

Posted Date: January 4th, 2022

DOI: <https://doi.org/10.21203/rs.3.rs-1153833/v1>

License:   This work is licensed under a Creative Commons Attribution 4.0 International License.

[Read Full License](#)

Version of Record: A version of this preprint was published at Biophysical Journal on February 1st, 2022.
See the published version at <https://doi.org/10.1016/j.bpj.2021.11.1084>.

Mapping the conformational energy landscape of Abl kinase using ClyA nanopore tweezers

Fanjun Li¹, Monifa A. Fahie², Kaitlyn Gilliam², Ryan Pham¹, and Min Chen^{1,2*}

¹Department of Chemistry and ²Molecular and Cellular Biology Program, University of Massachusetts Amherst, Amherst, MA 01003

* Corresponding Author:

Department of Chemistry, University of Massachusetts Amherst, Amherst MA 01003, USA

Email: mchen1@chem.umass.edu, Phone: 413-545-0683

Abstract

Protein kinases play central roles in cellular regulation by catalyzing the phosphorylation of target proteins. Kinases have inherent structural flexibility allowing them to switch between active and inactive states. Quantitative characterization of kinase conformational dynamics is challenging. Here we used nanopore tweezers to access the conformational dynamics of Abl kinase domain, which was shown to interconvert between two major conformational states where one conformation comprises three sub-states. Analysis of kinase-substrate and kinase-inhibitor interactions uncovered the functional roles of relevant states and enabled the elucidation of the mechanism underlying the catalytic deficiency of an inactive Abl mutant G321V. The energy landscape of Abl kinase was revealed by quantifying the population and transition rates of the conformational states.

Introduction

Protein kinases are attractive drug targets because they play a central role in regulating the majority of cellular pathways by catalyzing the phosphorylation of target proteins involved in complex physiological processes.¹ Abelson (Abl) kinase is a cytoplasmic tyrosine kinase. Dysregulated Abl kinase activity has been linked as a contributing factor in chronic myeloid leukemia (CML). Imatinib, an ATP-binding site inhibitor have been approved by FDA to treat CML.^{2, 3} However, the presence of mutations in advanced-stage patients render the drug ineffective,⁴⁻⁶ which has motivated the development of new therapeutics by modifying imatinib structure or exploring of alternative druggable states.^{7, 8}

Abl kinase has a conserved catalytic kinase domain, consisting of a N-terminal lobe (N-lobe) and a C-terminal lobe (C-lobe) that are linked by a flexible hinge. ATP binds to the cleft between the two lobes while the substrate protein/peptide binding site is located mainly at the C-lobe (**Fig. 1a**).⁹ ¹⁰ Conformational states of Abl kinase domain are usually classified according to the arrangement of four key elements including the activation loop (A-loop), the Asp-Phe-Gly motif (DFG-motif), the glycine rich loop (G-loop), and the α C-helix (**Fig. 1a**).^{11, 12} Biological functions of kinases are dictated by their structural flexibility switching between one active and multiple inactive states.¹³ Intermediate conformations emerging during state transitions could be potential druggable states.¹⁴ Therefore, comprehensive understandings of Abl conformational energy landscape, including structures, relative propensity of these states, and state transition kinetics, are desired. Despite a wealth of ligand-bound crystal structures of Abl are available, no crystal structure of *apo* Abl has been solved to date, which limits our understanding of possible conformations adopted by *apo* Abl. Recently, three *apo* Abl structures were solved with NMR at 10 °C in order to characterize the dynamics A-loop.¹⁵ Computational simulations have successfully identified some metastable states of *apo* Abl kinase^{12, 16}, but it remains challenging to obtain state transition kinetics owing to the large system size and long timescales associated with kinase conformational dynamics.^{17, 18}

Nanopore technology, having shown great success in DNA sequencing^{19, 20}, small molecules and proteins identification²¹⁻²⁵, is emerging as an attractive single-molecule tool for probing protein conformational dynamics^{26, 27}. Apart from the general strengths of single-molecule techniques such as the ability to access conformational heterogeneity, transient or sparsely populated intermediates, and sequential steps of enzyme's catalytic cycle²⁸⁻³², nanopore tweezers own some unique advantages including being label-free and capable of detecting structural dynamics in a wide range of timescales (μ s~mins).³³ Previous works showed that natively folded proteins^{26, 34-37} can be reversibly trapped with Cytolysin A (ClyA) nanopore variants to reveal their ligand bound and catalytic states. Notably, four different ionic states of dihydrofolate reductase (DHFR) were detected³⁴ and three anomeric maltose-bound states of maltose binding protein (MBP) were resolved by ClyA nanopores, the conformational difference among which was indicated however was not explicitly revealed by any structural studies.²⁶ Together, these works demonstrate the high spatial sensitivity of ClyA nanopore tweezers for resolving conformational states with subtle differences within flexible enzymes. Thus, in this study we used ClyA nanopore tweezers to track structural dynamics of the Abl kinase domain.

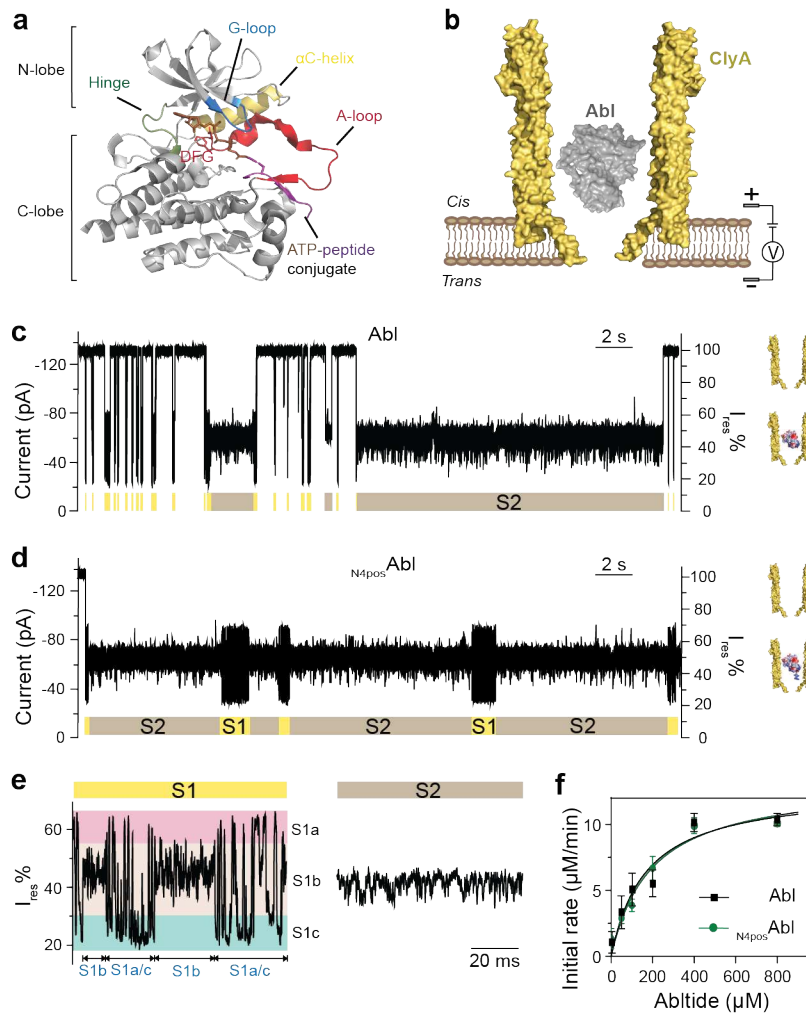


Fig. 1: Trapping of *apo* Abl kinases with ClyA-AS nanopore tweezers. **a**, Crystal structure of the catalytic domain of human Abl kinase (Abl, grey) bound with ATP-peptide conjugate (PDB: 2G1T). ATP in brown and peptide in purple. Structural elements are indicated with different colors, hinge in green, G-loop in blue, α C-helix in yellow, and A-loop in red. Side chain of DFG-motif is shown as stick. **b**, Schematic representation of a single catalytic domain of Abl kinase confined in a ClyA nanopore embedded in a planar lipid bilayer with negative applied potential at *trans*. **c-d**, Representative current traces and schematics of Abl (**c**) and $N_{4\text{pos}}$ Abl (**d**) trapped in a ClyA-AS nanopore. Signal pattern S1 (yellow), S2 (brown) are observed when Abl is trapped within nanopore. **e**, Zoomed in trace of S1 and S2 states from $N_{4\text{pos}}$ Abl trapping signal. Three sub-states were observed within S1, namely, S1a, S1b, and S1c. The state transition pathways were: $S1 \leftrightarrow S2$, $S1a/c \leftrightarrow S1b$, and $S1a \leftrightarrow S1c$. **f**, Michaelis-Menten kinetics analysis of Abl and $N_{4\text{pos}}$ Abl. The current traces were collected at -80 mV in 150 mM NaCl, 100 mM Tris-HCl, pH 7.5, with ~ 100 nM Abl kinase added to *cis* chamber, at 22 $^{\circ}\text{C}$.

Results and Discussions

Nanopore tweezers reveal multiple states of *apo* Abl kinase

Current recording experiments with ClyA-AS nanopore tweezers were performed on the catalytic domain of Abl kinase, termed Abl in this study to access the kinase conformational ensembles (**Fig. 1b**). Abl was driven to enter the nanopore by electroosmotic flow from *cis* to *trans*, resulting in a reduction in the ionic current I_{res} . Wildtype Abl kinase can be reversibly trapped under the applied potential of -80 mV (**Fig. 1c**) with a mean dwell time ($\tau_{trapping}$) of 0.06 ± 0.03 s (N=5), which is too short for monitoring the enzyme's conformational dynamics over multiple turnovers as the k_{cat} is 7.1 ± 0.7 s⁻¹ (**Supplementary Fig. 1, Supplementary Table 1**), requiring minimal 0.14 s to observe one catalytic cycle.

To extend the $\tau_{trapping}$, we introduced positively charged tags to Abl to enhance the electrophoretic force³⁸. We prepared two Abl constructs with a positively charged peptide tail at its N-terminus, termed N_{4pos} Abl, or to its C-terminus, named Abl_{C4pos} . Both Abl_{C4pos} and N_{4pos} Abl; showed longer $\tau_{trapping}$ of 1.52 ± 0.13 s (N=3) and 20.72 ± 2.83 s (N=3), respectively (**Fig. 1d, Supplementary Fig. 2, Supplementary Table 2**). Since N_{4pos} Abl exhibited the longest $\tau_{trapping}$, we decided to study this construct in detail. In current recording experiments, N_{4pos} Abl induced similar current signals as Abl (**Fig. 1c-e, Supplementary Fig. 3**). The current states are characterized by their relative residual current ($I_{res}\%$), state dwell time (τ), and state population (P) (**Supplementary Table 3**). *apo* N_{4pos} Abl generated two alternating current states (S1 and S2) with distinct signatures (**Fig. 1d-e**). The S2 state showed ~95% occupancy and a relative residue current $I_{res}\%$ ranging from 38-58%. The less populated S1 state (~5% occupancy) contained three distinct sub-states defined by the I_{res} : S1a, S1b and S1c. Notably, the three sub-states did not occur in a random manner. Instead, Abl alternately visited S1b and an S1a/c joint state. During the S1a/c joint state, Abl was found to oscillate rapidly between S1a and S1c. As a control, the Michaelis-Menten kinetic analysis demonstrated that the N-terminal positive tail had no influence on the catalytic activity (**Fig. 1f, Supplementary Table 1**).

In short, we obtained an active construct N_{4pos} Abl with increased dwell time to monitor the conformational dynamics of a single Abl over extended time. More importantly, we observed that the *apo* Abl kinase induced multiple current states in ClyA-AS nanopore tweezers.

S1 sub-states resemble substrate binding conformations

We next monitored the current signal of N_{4pos} Abl in the presence of various ligands³⁹. Firstly, addition of only MgCl₂ did not trigger any noticeable change (**Fig. 2a-b**), suggesting that the divalent cation did not perturb the ClyA/Abl system. In contrast, re-distributions of S1 sub-states were observed when different substrate/ligands were presented (**Fig. 2c-f, Supplementary Table 4**): A substrate peptide Abltide binding shifted the current state equilibrium to a pre-existing state S1b by increasing the relative occupancy $P_{S1b/S1}$ (defined as the population occupancy of S1b relative to S1) from $62.1 \pm 2.9\%$ to $93.6 \pm 0.3\%$ (**Fig. 2c**). Interestingly, ATP binding augmented a pre-existing S1a state by increasing $P_{S1a/S1}$ from $13.3 \pm 2.6\%$ to $19.3 \pm 2.2\%$. In addition, ATP also induced a new state S1d with a $P_{S1d/S1}$ of $39.8 \pm 2.1\%$ (**Fig. 2d**), indicating the existence of two ATP binding modes. As expected, binding of ATP to Abl kinase was Mg²⁺-dependent as *apo* N_{4pos} Abl signal was readily recovered after adding EDTA (**Supplementary Fig. 4**). Similar to ATP, ATPγS also stabilized S1a state and induced a new state S1d, although

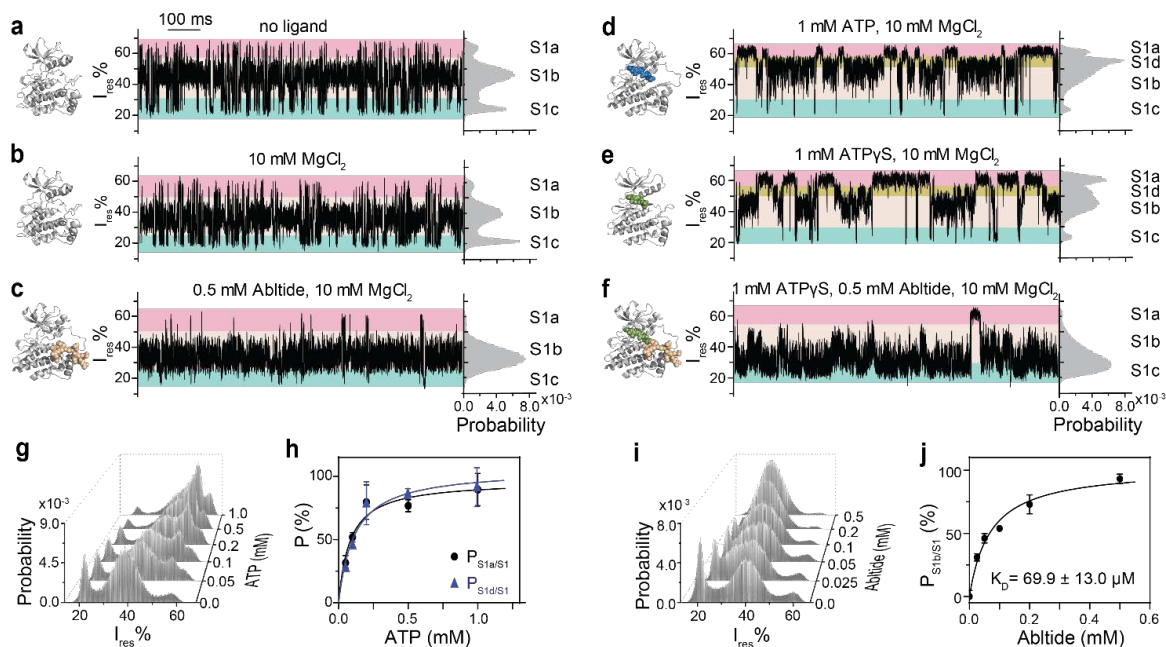


Fig. 2: Interactions of substrates and analogue with $N_{4\text{pos}}\text{Abl}$. a-f, Structural models, representative traces and corresponding histograms of S1 of *apo* $N_{4\text{pos}}\text{Abl}$ (a) and $N_{4\text{pos}}\text{Abl}$ in the presence of 10 mM MgCl_2 (b), 0.5 mM Abltide and 10 mM MgCl_2 (c), 1 mM ATP and 10 mM MgCl_2 (d), 1 mM ATPyS and 10 mM MgCl_2 (e), 0.5 mM Abltide, 1 mM ATPyS and 10 mM MgCl_2 (f). Structure models of *apo* Abl kinase domain and Abl:ATPyS were produced from PDB 6XR6 and 2G2F respectively. Structural models of Abl:ATP, Abl:Abltide and Abl:ATPyS:Abltide complexes were generated from PDB 2G1T. Abl, ATP, ATPyS and Abltide are colored in grey, blue, green and wheat, respectively. g, All points histograms of S1 states at various ATP concentration. h, Determination of K_D for ATP binding. i, All points histograms of S1 states at various Abltide concentration. j, Determination of K_D for Abltide binding. Three single nanopores were recorded for each concentration. All current traces were collected at -80 mV in 150 mM NaCl, 100 mM Tris-HCl, pH 7.5, at 22 °C.

showing a different population distribution: $P_{S1a/S1}$ of $30.0 \pm 2.0\%$ and $P_{S1d/S1}$ of $24.1 \pm 1.6\%$ (Fig. 2e). The ternary $N_{4\text{pos}}\text{Abl}/\text{ATP}/\text{Abltide}$ complex was mimicked by an $N_{4\text{pos}}\text{Abl}/\text{ATP}/\text{Abltide}$ state. The simultaneous binding of ATPyS and Abltide to $N_{4\text{pos}}\text{Abl}$ stabilized a pre-existing state S1c from $25.0 \pm 3.2\%$ to $37.9 \pm 2.5\%$ (Fig. 2f). Interestingly no obvious signal change was detected in S2 state for all ligands (Supplementary Fig. 5). The distribution of binding state populations was concentration dependent allowing the determination of the dissociation constants (K_D) for each ligand (Fig. 2g-j). The K_D was derived by fitting the relative population with the increasing ligand concentration as follows: $K_D^{\text{ATP}} = 81.6 \pm 17.9 \mu\text{M}$ (S1a binding mode), $112.9 \pm 25.3 \mu\text{M}$ (S1d binding mode), $K_D^{\text{Abltide}} = 69.9 \pm 13.0 \mu\text{M}$. Our K_D^{ATP} values are consistent with the reported $69 \pm 4 \mu\text{M}$.⁴⁰ No K_D value for this specific substrate peptide was determined previously.

Our data strongly indicate that S1 sub-states correspond to different ligand(s)-bound conformational states while S2 state reflects a conformation incapable of binding substrates. Also, the observation that *apo* Abl kinase can sample different ligand-bound states plus ATP homologues induced a new state suggest that Abl recognizes ligands through a combination of conformational selection and induced fit mechanisms.

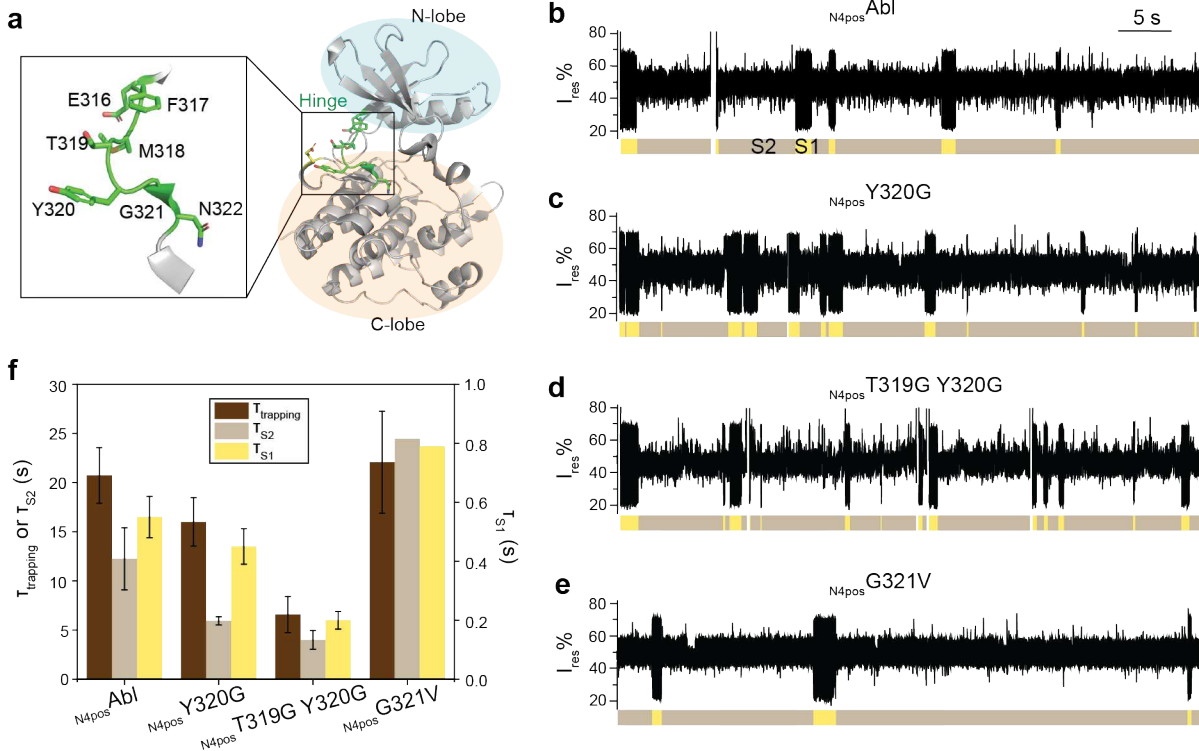


Fig. 3: Effect of Abl kinase hinge mutations on the S1/S2 state transitions. **a**, Structure of Abl kinase domain (grey, PDB: 2HYY) with hinge region colored in green. N-lobe and C-lobe are indicated by the pale blue and orange circles respectively. A magnified image shows the detailed hinge structure. **b-e**, Representative current traces of *apo* N_{4pos} Abl (**b**), N_{4pos} Y320G (**c**), N_{4pos} T319G Y320G (**d**) and N_{4pos} G321V (**e**) trapped with ClyA-AS nanopore tweezers. All current traces were collected at -80 mV in 150 mM NaCl, 100 mM Tris-HCl, pH 7.5, at 22 °C, with ~ 100 nM Abl kinase added to *cis* chamber. **f**, Comparison of the dwell times of trapping and S1, S2 states of different Abl hinge mutants.

S2 state is a non-ligand binding, lobe-open conformation

Conformational switch between lobe-open and -closed states have been observed in many protein kinases and shown to play an essential role in catalysis and kinase activation.⁴¹⁻⁴³ Structures of active states loaded with substrates have been shown to adopt a lobe-closed conformation while residues forming the catalytic cleft are further away at the lobe-open.^{44, 45} Here we suspected that the S1 state might represent lobe-closed conformations allowing ligand/substrate binding while the S2 state might be a lobe-open conformation incapable of ligand binding. Studies on extracellular signal-regulated kinase 2 (ERK2) suggested that the activation of ERK2 was promoted by increasing the flexibility of the hinge region that controls the N- and C-lobe domain movement.^{42, 43} To probe if S1/S2 states transition is related to the domain movement, mutations were introduced into the hinge region (Phe³¹⁷-Leu³²³) of Abl¹¹ to generate two mutants (N_{4pos} Y320G and N_{4pos} T319G Y320G) with increased flexibility, and one mutant (N_{4pos} G321V) with enhanced rigidity (**Fig. 3a**).

We then investigated how the hinge mutations affect the S1/S2 transition kinetics (**Fig. 3b-f**, **Supplementary Table 2**). Compared with N_{4pos} Abl, T_{S1} of N_{4pos} Y320G decreased by $\sim 18\%$ and T_{S2}

decreased by ~ 2 folds, suggesting a faster S1/S2 transition. For $N_{4\text{pos}}\text{T319G Y320G}$, τ_{S1} decreased by ~ 2.3 folds compared to $N_{4\text{pos}}\text{Y320G}$ and τ_{S2} by $\sim 32\%$, suggesting more rapid S1/S2 transitions were further promoted with the double glycine mutations. In contrast, both τ_{S1} (~ 0.79 s) and τ_{S2} (~ 24.46 s) of $N_{4\text{pos}}\text{G321V}$ showed an increase compared to $N_{4\text{pos}}\text{Abl}$, suggesting slower S1/S2 transitions. Interestingly, the trapping time decreased with the decreased hinge rigidity ($N_{4\text{pos}}\text{T319G Y320G} < N_{4\text{pos}}\text{Y320G} < N_{4\text{pos}}\text{Abl} < N_{4\text{pos}}\text{G321V}$), possibly due to the increased entropic cost of confining a more flexible protein within the nanopore (**Fig. 3f**). Together, all three mutants pointed out that the S1/S2 transition kinetics was sensitive to the hinge flexibility with a tendency that a more flexible hinge leads to faster transitions. Thus, our results strongly suggest that S1 and S2 states were induced by lobe motions with S1 likely resembling a lobe-closed conformation while S2 a lobe-open one.

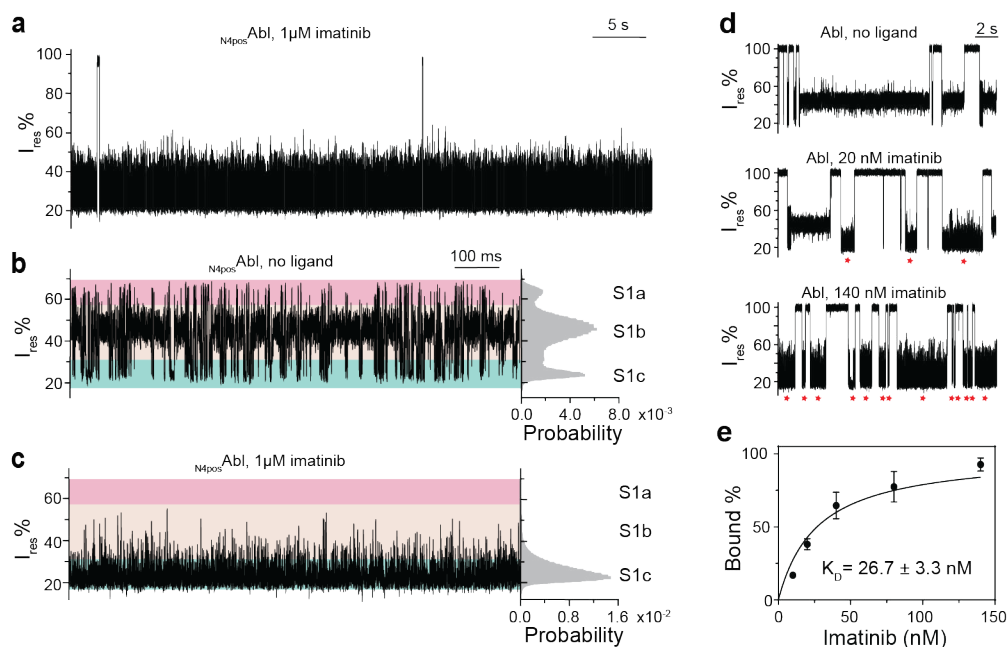


Fig. 4: Interaction of imatinib with Abl kinase. **a**, A representative trace of $N_{4\text{pos}}\text{Abl}$ trapped within ClyA-AS nanopore tweezers in the presence of $1 \mu\text{M}$ imatinib. **b-c**, Representative zoomed-in traces and corresponding histograms of *apo* $N_{4\text{pos}}\text{Abl}$ (**b**) and imatinib-bound $N_{4\text{pos}}\text{Abl}$ (**c**) observed with ClyA-AS nanopore tweezers. The current traces were collected at -80 mV in the buffer 150 mM NaCl, 100 mM Tris-HCl, pH 7.5 , at 22 $^{\circ}\text{C}$, with ~ 100 nM $N_{4\text{pos}}\text{Abl}$ added to *cis* chamber. **d**, Example traces of Abl titrated with different concentration of imatinib (0 , 20 nM, 140 nM). Red star indicates imatinib-bound Abl. The current traces were collected at -90 mV in the buffer 150 mM NaCl, 100 mM Tris-HCl, pH 7.5 , at 22 $^{\circ}\text{C}$, with ~ 100 nM Abl and different amount of imatinib added to *cis*. Three single nanopores were recorded for each concentration. **e**, Determination of imatinib dissociation constant K_D by plotting the imatinib-bound event population over imatinib concentration.

Imatinib stabilizes the S1c state

Imatinib has a slow k_{off} of $7.4 \times 10^{-4} \text{ s}^{-1}$, making it a useful tool to lock the protein in a specific conformational state.⁴⁶ In the presence of imatinib, the current traces no longer exhibited the hierarchical current states. Instead, the imatinib bound $N_{4\text{pos}}\text{Abl}$ triggered a noisy current pattern

showing a peak around the S1c state of *apo* $N_{4\text{pos}}$ Abl (**Fig. 4a-c**). The dwell time of $N_{4\text{pos}}$ Abl/imitinib complex was drastically increased to 103.9 ± 3.5 s ($N=2$), which is 100 times longer than the τ_{S1c} and 5 times longer than the trapping time of *apo* $N_{4\text{pos}}$ Abl. Our data indicated that imatinib binding stabilized a pre-existing conformational S1c state. Interestingly, the $N_{4\text{pos}}$ Abl/ATP γ S/Abtide ternary complex also appears to shift the equilibrium to S1c (**Fig. 4c, Fig. 2f**) despite two crystal structures showed that the activation loop of Abl/imitinib and Abl/ATP-peptide conjugate had closed and open conformations respectively (**Supplementary Fig. 6a**).^{47, 48} Note $N_{4\text{pos}}$ Abl/imitinib and $N_{4\text{pos}}$ Abl/ATP γ S/Abtide had distinct current patterns, both of which contained flickering events at ~ 200 μ s scale suggesting the existence of fast motions of dynamic components within these two types of ligand bound states (**Supplementary Fig. 6b-c**). Thus, we speculate that Abl/imitinib and Abl/ATP γ S/Abtide complexes within ClyA may share a large similarity in their conformations while the crystallization condition captured a snapshot of different conformational transitions for each ligand-bound complex. In addition, this result further supported that the S1c belonged to a lobe-closed or ligand-bound conformation. We also determined the K_D for imatinib binding to be 26.7 ± 3.3 nM (**Fig. 4d-e**), consistent with previously known values ranging from 1.5~47 nM.^{40, 49, 50}

Mechanism underlying the catalytic inactivity of Abl G321V

The G321V mutation abrogated the catalytic activity of Abl kinase by a mechanism unknown (**Supplementary Fig. 1**).⁵¹ Detailed examination of the current traces revealed that the $N_{4\text{pos}}$ G321V mutant generated a significantly different S1 sub-state distribution from that of $N_{4\text{pos}}$ Abl (**Fig. 5a-b, Supplementary Table 3**). The S1a of G321V became the dominating sub-state with an 80% occupancy of all S1 state compared with 17% for $N_{4\text{pos}}$ Abl, indicating that the G321V mutation not only altered the lobe-motions (S1/S2 transitions) but also affected the conformational distributions during the S1 lobe-closed state.

We next examined the ability of $N_{4\text{pos}}$ G321V to interact with substrates. Strikingly, addition of ATP (or ATP γ S) and MgCl₂ did not trigger any change in the current trace suggesting that $N_{4\text{pos}}$ G321V may be deficient in ATP binding (**Fig. 5c, Supplementary Fig. 7**). It was proposed that the ATP binding triggered assembling of a conserved hydrophobic spine, C-spine between the N- and C-lobe interface is crucial for kinase activity.⁵²⁻⁵⁵ The mutation G321V in ATP binding pocket was close to the residues constituting the C-spine (**Fig. 5e**). Because G321V exhibited an increased S1a sub-state, we speculate that G321V mutation may enhance hydrophobic interactions of the C-spine residues and promote the assembling of the C-spine to mimic an ATP-like binding state in the absence of ATP (**Fig. 5a-b**). In addition, the bulkier side chain of V321 could clash with the ribose group of ATP, making ATP geometrically unfit for the mutated ATP-binding pocket. We also tested the binding ability of $N_{4\text{pos}}$ G321V to Abtide (**Fig. 5a, Fig. 5d**). Interestingly, the K_D^{Abtide} of $N_{4\text{pos}}$ G321V (257.3 ± 55.9 μ M) decreased by ~ 3.7 folds compared with that of $N_{4\text{pos}}$ Abl despite the lack of direct contact between G321V and Abtide, suggesting the hinge region allosterically regulates peptide binding (**Fig. 5f**). Together, these results strongly pointed out that the loss of catalytic activity of G321V mutant was due to its inability in ATP binding.

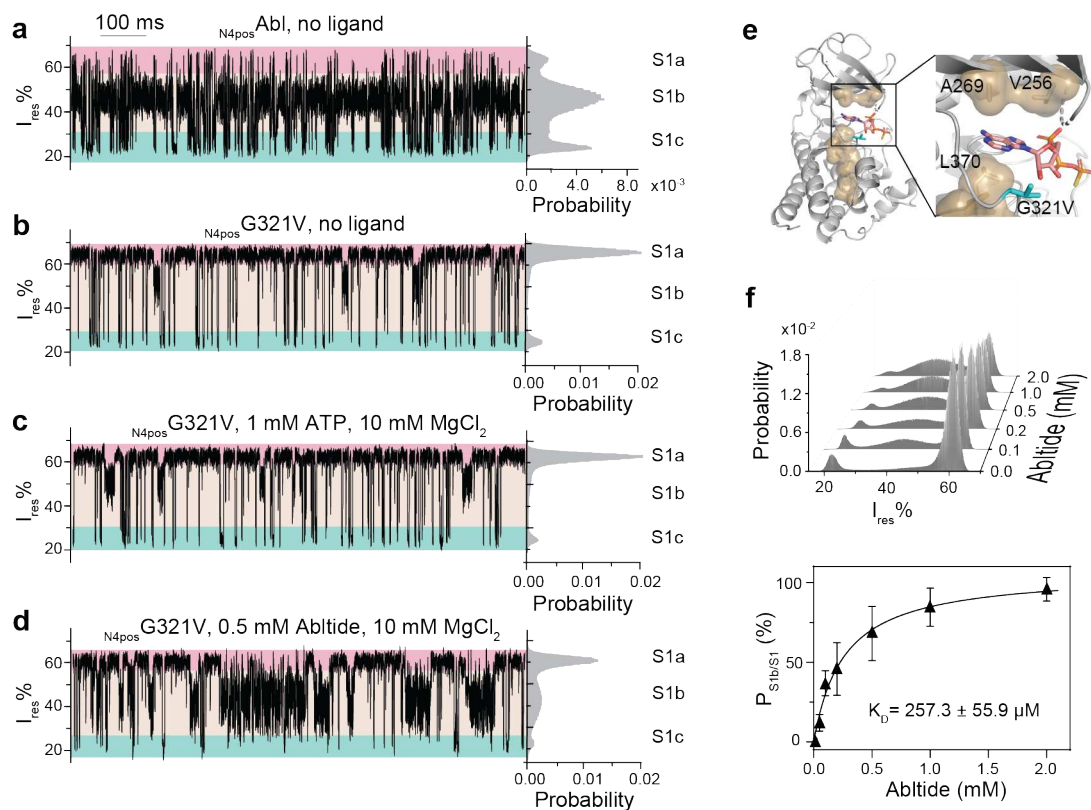


Fig. 5: Trapping of catalytic inactive G321V mutant with ClyA-AS nanopore tweezers. a-d, Representative S1 state traces and corresponding histograms of *apo* N_{4pos}Abl (**a**), *apo* N_{4pos}G321V (**b**) and N_{4pos}G321V in the presence of 1 mM ATP and 10 mM MgCl₂ (**c**), 0.5 mM Abltide and 10 mM MgCl₂ (**d**). **e**, Structure of G321V modeled from ATPγS-bound wildtype Abl kinase structure (PDB ID: 2G2F). ATPγS is shown as stick with carbon atoms colored in pink. G321V mutation is shown as stick and colored in cyan. Hydrophobic residues forming the C-spine are shown in surface model and highlighted in sand color, V256, A269 and L370 are close to the ATP/ATPγS binding site. **f**, Histogram of S1 state for Abltide titration to N_{4pos}G321V (top). Determination of the binding affinity of Abltide to N_{4pos}G321V based on the S1 state histograms (bottom). Three single nanopores were recorded for each concentration. The current traces were collected at -80 mV in buffer 150 mM NaCl, 100 mM Tris-HCl, pH 7.5, at 22 °C.

The conformational energy landscapes of *apo* N_{4pos}Abl

Our nanopore tweezers showed that the *apo* Abl kinases exhibit an ensemble of conformational states in solution. Quantification of the thermodynamic and kinetic parameters of those conformations enabled us to propose a comprehensive conformational energy landscape model for N_{4pos}Abl (**Fig. 6, Supplementary Table 5**). There are two main basins in the energy landscapes of *apo* N_{4pos}Abl corresponding to two main conformational states, one higher-energy lobe-closed conformation (S1) and the other lower-energy lobe-open conformation (S2). The transition rate constant from S1 to S2 state or lobe open rate constant ($k_{S1 \rightarrow S2}$) was $1.86 \pm 0.24 \text{ s}^{-1}$ and lobe close rate constant ($k_{S2 \rightarrow S1}$) was $0.09 \pm 0.24 \text{ s}^{-1}$. The free energy difference between S1 and S2 state ($\Delta G_{S1, S2}$) was $7.57 \pm 0.91 \text{ KJ} \cdot \text{mol}^{-1}$. Inside the basin S1, there are three sub-basins (a, b, c) separated by smaller energy barriers, corresponding to three conformational sub-states,

S1a, S1b and S1c, which resemble different substrate binding states (**Fig. 2**). The transition rate constants of $k_{S1a/c \rightarrow S1b}$ and $k_{S1b \rightarrow S1a/c}$ was 154.1 s^{-1} and 97.9 s^{-1} respectively. Notably, S1a and S1c share nearly equal free energy with a very small $\Delta G_{S1a, S1c}$ ($0.42 \pm 0.21 \text{ KJ}^* \text{ mol}^{-1}$). The S1a and S2c states also show rapid transitions ($k_{S1a \rightarrow S1c} = 974 \text{ s}^{-1}$ and $k_{S1c \rightarrow S1a} = 824 \text{ s}^{-1}$).

In comparison, a recent NMR study performed at $10 \text{ }^\circ\text{C}$ showed that *apo* Abl kinase interconverted between three states linearly, $G \leftrightarrow E1 \leftrightarrow E2$.¹⁵ The G state dominated the population by 88% while E1 and E2 had a population of 6% for each. Using the ^{13}C -based chemical exchange saturation transfer (CEST), the exchange rate (k_{ex}) for the $G \leftrightarrow E1$ transition and $E1 \leftrightarrow E2$ transition were determined as $46.8 \pm 4.3 \text{ s}^{-1}$ and $88.7 \pm 13.5 \text{ s}^{-1}$, respectively.¹⁵ Note, the lobe close and open motion revealed by our nanopore tweezers at room temperature has a slow rate ($k_{S2 \rightarrow S1} = 0.09 \pm 0.02 \text{ s}^{-1}$, $k_{S1 \rightarrow S2} = 1.86 \pm 0.24 \text{ s}^{-1}$). At $10 \text{ }^\circ\text{C}$, such motion would further slowdown, which likely becomes invisible in the ^{13}C -based CEST measurements that focused on the time scale between ~ 20 and 500 s^{-1} .⁵⁶ Interestingly, the transition rates of three sub-states in our nanopore measurements fell well in the detection range of the NMR study. Therefore, we propose that the three sub-states S1a, S1c and S1b may correlate with the G, E1 and E2 conformers whose structures differ mainly in the arrangement of the A-loop, DFG and the αC -helix.

Current signal fluctuations of the trapped protein could have two origins: 1) alteration of the protein-ClyA interface caused by the conformational changes of the protein; 2) metastable protein/nanopore interactions, e.g. protein moves between different sites of lumen or tumbling inside of nanopore. Multiple pieces of evidence supported that the observed current states were induced by kinase conformational changes. First, the binding of different substrates or substrate combination stabilized unique pre-existing S1 sub-states of *apo* $\text{N}_{4\text{pos}}$ Abl (S1a, S1b, S1c), suggesting that the S1 sub-states resembled the substrate binding conformations. Second, substitution of hinge residues of Abl kinase to non-charged amino acids (Y320G, G321V, and T319G Y320G) altered the population and dwell time of S1 and S2 states, suggesting that both S1 and S2 were associated with conformational states that were regulated by the hinge motions of the kinase. Particularly, the faster S1/S2 transition rates of these mutants were tightly correlated with the increasing flexibility of the hinge. Third, after saturating the kinase with imatinib, the S1a, S1b, and S2 states were depleted and the Abl/imatinib complex exhibited current levels close to the S1c state. Together, our data strongly indicate that *apo* Abl kinase interconverted between two major conformations and three conformational sub-states. Further analysis will be carried out to explore how ligands, inhibitor molecules and drug-resistant mutations modulate the conformational landscapes of Abl kinase in the future.

Here we have demonstrated nanopore tweezers that can measure structural dynamics at a broad time scale ($100 \mu\text{s} \sim \text{hr}$) while still maintain a high temporal resolution at $100 \mu\text{s}$. More importantly, nanopore devices could operate in high throughput with massive multiplexing capabilities at low-cost.⁵⁷ Thus, we expect nanopore tweezers to be a paradigm shift that will expand the single-molecule protein structural dynamic studies from the realm of fundamental research in specialized

laboratories toward more broad areas in drug discovery, medical diagnostics and precision medicine.

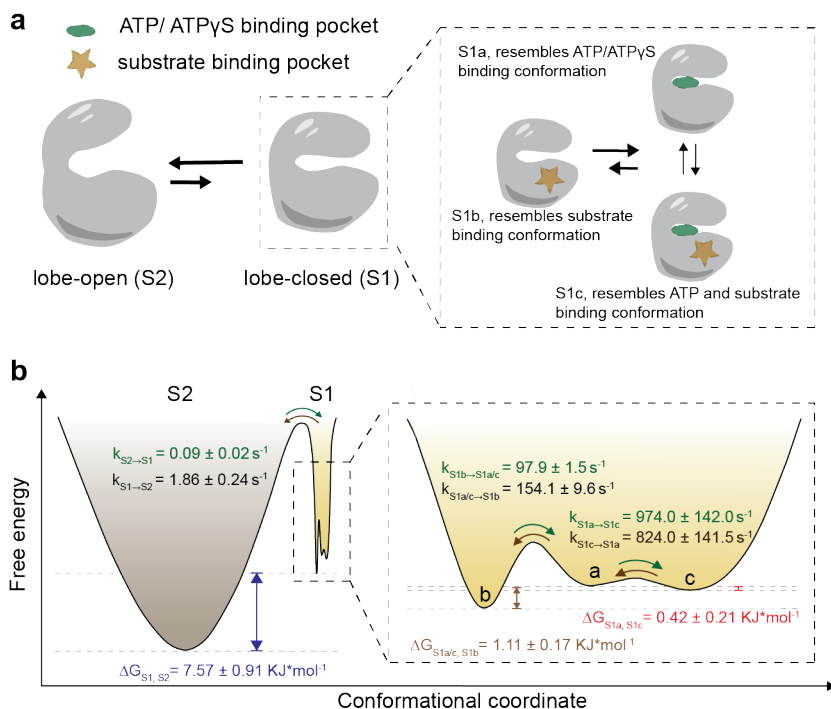


Fig. 6: Conformational dynamics of apo Abl kinase domain. **a**, Model of apo Abl kinase domain conformational changes. Two major conformations (S1: lobe-closed, S2: lobe-open) and three S1 conformational sub-states (S1a, S1b, S1c) which resemble substrate or substrate combination binding states are observed. **b-c**, Schematics of the conformational energy landscape of apo N4posAbl (**b**) and N4posG321V (**c**). S1 (yellow) and S2 (brown) indicate the two major conformations, lobe-closed and lobe-open, respectively. S1 conformational sub-states, S1a, S1b, S1c are indicated by a, b, c, respectively. Transition rate constant (k), and free energy difference (ΔG) between states are shown on the graphs.

Conclusions:

In this study we have applied ClyA nanopore tweezers to reveal a comprehensive conformational energy landscape of the Abl kinase domain and its interactions with other ligands. Our work also paves the way for further development of nanopore tweezers as an emerging transformative technology in fundamental research and medical applications.

Materials and Methods

Mutagenesis, expression, and purification of Abl kinase

Wild-type Abl kinase was expressed and purified as described previously.⁵⁸ Briefly, the Abl kinase containing plasmid pET_His10 TEV_ and the YopH phosphatase containing plasmid pET_YopH (residues 164-468) were co-transformed to BL21(DE3)pLysS competent cells for protein expression. Both plasmids pET His10 TEV_Abl (Addgene plasmid # 79727) and pET_YopH (residues 164-468) (Addgene plasmid # 79749) were gifts from John Chodera & Nicholas

Levinson & Markus Seeliger. Co-expression with the YopH phosphatase is to prevent potential autophosphorylation of Abl kinase. Cells were grown in 2xYT media at a 37° C shaker until OD_{600nm} reached 0.8~1. Cells were then induced with 0.25mM isopropyl β-D-1-thiogalactopyranoside (IPTG) for 16 hours at 16° C. Afterwards, cells were harvested and resuspended in lysis buffer (50 mM TrisHCl, 150 mM NaCl, 5% glycerol, pH 8) and lysed via sonicator (Misonix). The cells were pelleted by centrifugation at 20 000 g for 20 min at 4 °C, and the supernatant was purified with Ni-NTA affinity chromatography. The proteins were washed with buffer containing 50 mM Tris-HCl, pH 8, 500 mM NaCl, 75 mM imidazole, 5% glycerol and eluted in buffer containing 50 mM Tris-HCl, pH 8, 500 mM NaCl, 200 mM imidazole, 5% glycerol. TEV protease was added to the elutions from Ni-NTA with a mole ratio of 1:15 (TEV:kinase) to remove the His-tag while dialyzed for 16 hours at 4° C in dialysis buffer (50 mM TrisHCl, 100 mM NaCl, 5% glycerol, 1 mM DTT, pH 8). The dialyzed solution was then applied to an anion exchange column to remove TEV and phosphatase. The proteins were washed with buffer containing 50 mM Tris-HCl, pH 8, 100 mM NaCl, 5% glycerol, 1mM DTT and eluted in buffer containing 50 mM Tris-HCl, pH 8, 200 mM NaCl, 5% glycerol, 1mM DTT. The elute from anion exchange purification was concentrated by centricon with 10 000 Da cutoff and loaded to a size-exclusion column (HW5SS, GE Healthcare Life Sciences) to remove potential aggregates with running buffer (50 mM TrisHCl, 150 mM NaCl, 5% glycerol, 1 mM DTT, pH 8). Different Abl mutants were generated with mutagenesis primers listed in **Supplementary Table 6**. All Abl kinase mutants were expressed and purified in a similar fashion as wild-type Abl. The purity of Abl proteins was examined by 12% sodium-dodecyl sulfate polyacrylamide gel electrophoresis (SDS-PAGE) (**Supplementary Fig. 8**).

Abl Kinase assay

The activities of Abl proteins were measured using an enzyme-coupled assay as described before⁵⁸, where the consumption of NADH (absorption at 340 nm) correlated to the phosphate transfer. Reactions were performed at 30° C with 30 nM kinase, 10 mM MgCl₂, 100 mM Tris (pH 8.0), 2.2 mM ATP, 1 mM phosphoenolpyruvate, 0.6 mg/mL NADH, 75 U/mL pyruvate kinase, 105 U/mL lactate dehydrogenase, and 0.5 mM kinase substrate peptide Abltide (sequence: KKGEAIYAAPFA). Absorbance at 340 nm was monitored with a microtiter plate spectrophotometer (BioTek Synergy 2) for 20 min. The background kinase activity was determined in reaction mix without the substrate peptide and subtracted from the experiments with the substrate peptide. To obtain the enzyme kinetics, initial phosphorylation rates at different substrate peptide concentration (50~800 μM) were measured. Plots of initial rate as a function of peptide substrate concentration were fit by nonlinear regression to obtain the Michaelis-Menten kinetic parameters.

Preparation of ClyA-AS nanopore

ClyA-AS monomer was expressed and purified as described previously.⁵⁹ Briefly, ClyA-AS containing plasmid pET3a-his6-ClyA-AS was transformed into BL21(DE3) *E. coli* competent cells for protein expression. Cells were grown in LB media at 37°C until OD₆₀₀ reached ~0.6. Then IPTG was added with a final concentration of 0.5 mM to induce the cells and incubated at 16°C for ~16 hours. The cells were harvested and resuspended in lysis buffer (50 mM TrisHCl, 150 mM NaCl, 5% glycerol, pH 8) and lysed via sonicator (Misonix). The cells were pelleted by centrifugation at 20 000 g for 20 min at 4 °C. The supernatant was then purified with gravity Ni-

NTA affinity columns equilibrated with buffer containing 150 mM NaCl, 20mM imidazole, 50 mM TrisHCl, pH 8. Wash buffer (150 mM NaCl, 100mM imidazole, 50 mM TrisHCl, pH 8) was then applied to the column to wash off impurities. The ClyA-AS was eluted with elution buffer (150 mM NaCl, 200mM imidazole, 50 mM TrisHCl, pH 8). The elution from Ni-NTA columns was further purified by a size-exclusion column (HW5SS, GE Healthcare Life Sciences) with running buffer (150 mM NaCl, 50 mM TrisHCl, pH 8) to remove the potential aggregates. Proteins were frozen in liquid nitrogen and stored at -80C for future use. The ClyA-AS monomer was assembled into oligomer by incubating with 1% DDM at room temperature for 30 min and then stored in a 4 °C fridge for current recording experiments.

Single-channel current recording and data analysis

Single-channel current recording was performed using a similar protocol at room temperature 22°C as previously described.²⁶ Briefly, a ClyA-AS nanopore was inserted into a DPhPC lipid bilayer separating two chambers. Both chambers were filled with 300 μ L buffer (150 mM NaCl, 100 mM Tris-HCl, pH 7.5). ClyA-AS was added to the cis chamber that was grounded and then spontaneously inserted into the bilayer. Abl kinase (~100 nM) was added to the same chamber. After applying a negative voltage bias across the bilayer, the current generated by the ions flow through the nanopore was monitored in voltage-clamp mode by an integrated patch clamp amplifier (Axopatch 200B, Molecular Devices). The current signal was acquired by an analog-to-digital converter (Digidata 1440A, Molecular Devices) at a sampling rate of 50 kHz after processing with a 4-pole lowpass Bessel filter at 2 kHz. Data were recorded by Clampex software (Molecular Devices).

Residual current ($I_{res}\%$) was calculated from blocked pore current (I_B) and open pore current (I_O) with $I_{res}\% = 100 \cdot I_B / I_O$. State dwell time (τ) for each experiment was determined by using “single-channel search” in Clampfit. All event dwell times from one nanopore experiment were binned together as a conventional distribution and fitted to a standard single-exponential function to derive the τ for that specific state. The average τ and standard deviation were determined from three independent ClyA-AS nanopore measurements. Of note in calculating τ_{S1} and τ_{S2} , the S1 or S2 states at the beginning and those at the end of a trapping event were discarded as their true dwell times were interrupted by Abl entering and exiting the ClyA-AS nanopore. However, due to the super slow transition between S1 and S2 in $N_{4pos}G321V$, we were not able to collect enough complete S1, S2 states for a good single-exponential fitting from one experiment. Therefore, all complete S1 or S2 from multiple experiments were combined to derive the τ_{S1} and τ_{S2} for $N_{4pos}G321V$. Consequently, we were not able to derive standard deviation for τ_{S1} and τ_{S2} for $N_{4pos}G321V$. State transition rate constant (k) was calculated with equation: $k = 1/\tau$. For example, the transition rate constant from S1 to S2 state, $k_{S1 \rightarrow S2} = 1/\tau_{S1}$. State population (P) was calculated either by state dwell times, for example, $P_{S1} = \tau_{S1} / (\tau_{S1} + \tau_{S2})$. Relative state occupancy in the presence of different ligands was calculated by peak area in histograms. The dissociation constant (K_D) of the ATP or Abltide from Abl kinase was determined from titration experiments. Plots of bound state occupancy as a function of titrate (ATP or Abltide) concentration were fit by nonlinear regression with single site binding model to obtain K_D .

Acknowledgements:

Plasmid pET3a-his6-ClyA-AS was a generous gift from Dr. Giovanni Maglia. Research in the Chen lab was supported by grants R01GM115442 and R01AI156187 from NIH. We appreciate all valuable discussions with Prof. Margaret Stratton, Dr. Bach Pham, Dr. Xin Li, Dr. Jiale Du, Dr. Kirandeep Deol, Dr. Meizhe Wang, Dr. Patanachai 'Kong' Limpikirati and Senyao He.

References

1. Druker, B.J. & Lydon, N.B. Lessons learned from the development of an abl tyrosine kinase inhibitor for chronic myelogenous leukemia. *J Clin Invest* **105**, 3-7 (2000).
2. Schindler, T. et al. Structural mechanism for STI-571 inhibition of abelson tyrosine kinase. *Science* **289**, 1938-1942 (2000).
3. Noble, M.E., Endicott, J.A. & Johnson, L.N. Protein kinase inhibitors: insights into drug design from structure. *Science* **303**, 1800-1805 (2004).
4. Roumiantsev, S. et al. Clinical resistance to the kinase inhibitor STI-571 in chronic myeloid leukemia by mutation of Tyr-253 in the Abl kinase domain P-loop. *Proc Natl Acad Sci U S A* **99**, 10700-10705 (2002).
5. Leguay, T. et al. An amino-acid switch in the BCR-ABL kinase domain modifies sensitivity to imatinib mesylate. *Leukemia* **19**, 1671-1673 (2005).
6. Melo, J.V. & Chuah, C. Resistance to imatinib mesylate in chronic myeloid leukaemia. *Cancer Lett* **249**, 121-132 (2007).
7. Weisberg, E. et al. AMN107 (nilotinib): a novel and selective inhibitor of BCR-ABL. *Br J Cancer* **94**, 1765-1769 (2006).
8. Wylie, A.A. et al. The allosteric inhibitor ABL001 enables dual targeting of BCR-ABL1. *Nature* **543**, 733-737 (2017).
9. Panjarian, S., Iacob, R.E., Chen, S., Engen, J.R. & Smithgall, T.E. Structure and dynamic regulation of Abl kinases. *J Biol Chem* **288**, 5443-5450 (2013).
10. Taylor, S.S. & Kornev, A.P. Protein kinases: evolution of dynamic regulatory proteins. *Trends Biochem Sci* **36**, 65-77 (2011).
11. Vajpai, N. et al. Solution conformations and dynamics of ABL kinase-inhibitor complexes determined by NMR substantiate the different binding modes of imatinib/nilotinib and dasatinib. *J Biol Chem* **283**, 18292-18302 (2008).
12. Paul, F., Meng, Y. & Roux, B. Identification of Druggable Kinase Target Conformations Using Markov Model Metastable States Analysis of apo-Abl. *J Chem Theory Comput* **16**, 1896-1912 (2020).
13. Tong, M. & Seeliger, M.A. Targeting conformational plasticity of protein kinases. *ACS Chem Biol* **10**, 190-200 (2015).
14. Shukla, D., Meng, Y., Roux, B. & Pande, V.S. Activation pathway of Src kinase reveals intermediate states as targets for drug design. *Nat Commun* **5**, 3397 (2014).
15. Xie, T., Saleh, T., Rossi, P. & Kalodimos, C.G. Conformational states dynamically populated by a kinase determine its function. *Science* **370** (2020).
16. Narayan, B. et al. The transition between active and inactive conformations of Abl kinase studied by rock climbing and Milestoning. *Biochim Biophys Acta Gen Subj* **1864**, 129508 (2020).
17. Orellana, L. Large-Scale Conformational Changes and Protein Function: Breaking the in silico Barrier. *Front Mol Biosci* **6**, 117 (2019).
18. Kornev, A.P. & Taylor, S.S. Dynamics-Driven Allostery in Protein Kinases. *Trends Biochem Sci* **40**, 628-647 (2015).
19. Manrao, E.A. et al. Reading DNA at single-nucleotide resolution with a mutant MspA nanopore and phi29 DNA polymerase. *Nat Biotechnol* **30**, 349-353 (2012).

20. Deamer, D., Akeson, M. & Branton, D. Three decades of nanopore sequencing. *Nat Biotechnol* **34**, 518-524 (2016).
21. Fahie, M., Chisholm, C. & Chen, M. Resolved single-molecule detection of individual species within a mixture of anti-biotin antibodies using an engineered monomeric nanopore. *ACS Nano* **9**, 1089-1098 (2015).
22. Pham, B. et al. A Nanopore Approach for Analysis of Caspase-7 Activity in Cell Lysates. *Biophys J* **117**, 844-855 (2019).
23. Ramsay, W.J. & Bayley, H. Single-Molecule Determination of the Isomers of d-Glucose and d-Fructose that Bind to Boronic Acids. *Angew Chem Int Ed Engl* **57**, 2841-2845 (2018).
24. Harrington, L., Alexander, L.T., Knapp, S. & Bayley, H. Pim Kinase Inhibitors Evaluated with a Single-Molecule Engineered Nanopore Sensor. *Angew Chem Int Ed Engl* **54**, 8154-8159 (2015).
25. Li, W. et al. Single protein molecule detection by glass nanopores. *ACS Nano* **7**, 4129-4134 (2013).
26. Li, X., Lee, K.H., Shorkey, S., Chen, J. & Chen, M. Different Anomeric Sugar Bound States of Maltose Binding Protein Resolved by a Cytolysin A Nanopore Tweezer. *ACS Nano* **14**, 1727-1737 (2020).
27. Schmid, S., Stommer, P., Dietz, H. & Dekker, C. Nanopore electro-osmotic trap for the label-free study of single proteins and their conformations. *Nat Nanotechnol* **16**, 1244-1250 (2021).
28. Lerner, E. et al. Toward dynamic structural biology: Two decades of single-molecule Forster resonance energy transfer. *Science* **359** (2018).
29. Aviram, H.Y. et al. Direct observation of ultrafast large-scale dynamics of an enzyme under turnover conditions. *Proc Natl Acad Sci U S A* **115**, 3243-3248 (2018).
30. Neuman, K.C. & Nagy, A. Single-molecule force spectroscopy: optical tweezers, magnetic tweezers and atomic force microscopy. *Nat Methods* **5**, 491-505 (2008).
31. Gupta, A.N. et al. Experimental validation of free-energy-landscape reconstruction from non-equilibrium single-molecule force spectroscopy measurements. *Nature Physics* **7**, 631-634 (2011).
32. Comstock, M.J. et al. Protein structure. Direct observation of structure-function relationship in a nucleic acid-processing enzyme. *Science* **348**, 352-354 (2015).
33. Schmid, S. & Dekker, C. Nanopores: a versatile tool to study protein dynamics. *Essays Biochem* **65**, 93-107 (2021).
34. Galenkamp, N.S., Biesemans, A. & Maglia, G. Directional conformer exchange in dihydrofolate reductase revealed by single-molecule nanopore recordings. *Nat Chem* **12**, 481-488 (2020).
35. Galenkamp, N.S., Soskine, M., Hermans, J., Wloka, C. & Maglia, G. Direct electrical quantification of glucose and asparagine from bodily fluids using nanopores. *Nat Commun* **9**, 4085 (2018).
36. Van Meervelt, V., Soskine, M. & Maglia, G. Detection of two isomeric binding configurations in a protein-aptamer complex with a biological nanopore. *ACS Nano* **8**, 12826-12835 (2014).
37. Lu, B. et al. Protein Motion and Configurations in a Form-Fitting Nanopore: Avidin in ClyA. *Biophys J* **115**, 801-808 (2018).
38. Willems, K. et al. Engineering and Modeling the Electrophoretic Trapping of a Single Protein Inside a Nanopore. *ACS Nano* **13**, 9980-9992 (2019).
39. Levinson, N.M. & Boxer, S.G. Structural and spectroscopic analysis of the kinase inhibitor bosutinib and an isomer of bosutinib binding to the Abl tyrosine kinase domain. *PLoS One* **7**, e29828 (2012).

40. Hoemberger, M., Pitsawong, W. & Kern, D. Cumulative mechanism of several major imatinib-resistant mutations in Abl kinase. *Proc Natl Acad Sci U S A* **117**, 19221-19227 (2020).
41. Masterson, L.R. et al. Dynamics connect substrate recognition to catalysis in protein kinase A. *Nat Chem Biol* **6**, 821-828 (2010).
42. Sours, K.M., Xiao, Y. & Ahn, N.G. Extracellular-regulated kinase 2 is activated by the enhancement of hinge flexibility. *J Mol Biol* **426**, 1925-1935 (2014).
43. Xiao, Y. et al. Phosphorylation releases constraints to domain motion in ERK2. *Proc Natl Acad Sci U S A* **111**, 2506-2511 (2014).
44. Zheng, J. et al. 2.2 Å refined crystal structure of the catalytic subunit of cAMP-dependent protein kinase complexed with MnATP and a peptide inhibitor. *Acta Crystallogr D Biol Crystallogr* **49**, 362-365 (1993).
45. Akamine, P. et al. Dynamic Features of cAMP-dependent Protein Kinase Revealed by Apoenzyme Crystal Structure. *Journal of Molecular Biology* **327**, 159-171 (2003).
46. Liang, W. et al. Measurement of small molecule binding kinetics on a protein microarray by plasmonic-based electrochemical impedance imaging. *Anal Chem* **86**, 9860-9865 (2014).
47. Levinson, N.M. et al. A Src-like inactive conformation in the abl tyrosine kinase domain. *PLoS Biol* **4**, e144 (2006).
48. Cowan-Jacob, S.W. et al. Structural biology contributions to the discovery of drugs to treat chronic myelogenous leukaemia. *Acta Crystallogr D Biol Crystallogr* **63**, 80-93 (2007).
49. Shan, Y. et al. A conserved protonation-dependent switch controls drug binding in the Abl kinase. *Proc Natl Acad Sci U S A* **106**, 139-144 (2009).
50. Kwarcinski, F.E. et al. Conformation-Selective Analogues of Dasatinib Reveal Insight into Kinase Inhibitor Binding and Selectivity. *ACS Chem Biol* **11**, 1296-1304 (2016).
51. Balzano, D., Santaguida, S., Musacchio, A. & Villa, F. A general framework for inhibitor resistance in protein kinases. *Chem Biol* **18**, 966-975 (2011).
52. Kim, J. et al. A dynamic hydrophobic core orchestrates allostery in protein kinases. *Sci Adv* **3**, e1600663 (2017).
53. McClendon, C.L., Kornev, A.P., Gilson, M.K. & Taylor, S.S. Dynamic architecture of a protein kinase. *Proc Natl Acad Sci U S A* **111**, E4623-4631 (2014).
54. Kornev, A.P., Haste, N.M., Taylor, S.S. & Ten Eyck, L.F. Surface comparison of active and inactive protein kinases identifies a conserved activation mechanism. *Proceedings of the National Academy of Sciences* **103**, 17783-17788 (2006).
55. Hu, J. et al. Kinase regulation by hydrophobic spine assembly in cancer. *Mol Cell Biol* **35**, 264-276 (2015).
56. Vallurupalli, P., Sekhar, A., Yuwen, T. & Kay, L.E. Probing conformational dynamics in biomolecules via chemical exchange saturation transfer: a primer. *J Biomol NMR* **67**, 243-271 (2017).
57. Kono, N. & Arakawa, K. Nanopore sequencing: Review of potential applications in functional genomics. *Dev Growth Differ* **61**, 316-326 (2019).
58. Seeliger, M.A. et al. High yield bacterial expression of active c-Abl and c-Src tyrosine kinases. *Protein Sci* **14**, 3135-3139 (2005).
59. Soskine, M., Biesemans, A., De Maeyer, M. & Maglia, G. Tuning the size and properties of ClyA nanopores assisted by directed evolution. *J Am Chem Soc* **135**, 13456-13463 (2013).

Supplementary Files

This is a list of supplementary files associated with this preprint. Click to download.

- [SupportingClyAAbl.pdf](#)